

Supporting information for

Data-Driven Recursive Kinetic Modeling for Fenton Reaction

Tian-Wei Hua¹, Gui-Xiang Huang^{1,*}, Chen Qian¹, Hou-Wei Zeng¹, Jun Jiang², Han-

Qing Yu^{1,*}

¹State Key Laboratory of Advanced Environmental Technology, Department of
Environmental Science and Engineering, University of Science and Technology of
China, Hefei, 230026, China

²Hefei National Research Center for Physical Sciences at the Microscale, School of
Chemistry and Materials Science, University of Science and Technology of China,
Hefei 230026, China

This supporting information contains 58-page document, including 6 texts, 22 figures,
17 tables, references and this cover page.

Supplementary Text

S1. Complex impacts of the conditions on reaction

Reaction conditions, including the concentrations of reactants (Fe^{2+} , H_2O_2 and organic reactant), as well as the type of organic reactant, have significant impacts on the performance of Fenton reactions.

Before analyzing the impacts, a systematic examination of the remaining concentrations' distribution within the dataset was conducted to avoid the potential biases caused by the data distribution. As shown in Figure S1a, the remaining concentrations at the first sampling point approximately followed a normal distribution, indicating a random and unbiased sampling process. As shown in Figure S1b, the remaining concentrations at all sampling points did not conform to a normal distribution. This can be attributed to that we want most reactions to achieve a high reactant conversion, thus leading to a denser data distribution of high conversions.

S1.1 Impact of reactant concentration on reaction

The effect of reactant concentrations on reaction was first analyzed. To comprehensively assess their influence on the entire reaction process, the remaining concentration of the organic reactant at the last sampling time (i.e., 30 min) was selected as the performance metric for the reactions. Furthermore, the individual influence of reactant concentrations was approximately estimated by normalizing the influence of the organic reactant type using the following equation:

$$I(RC) = \frac{1}{n} \sum_{i=1}^n C(RC, ort_i) \quad (1)$$

where I denotes the influence of reactant concentrations or organic reactant types. RC and ort are a variable representing the reactant concentrations and a specific type of organic reactant, respectively.

As illustrated in Figure S2, the remaining concentration of the organic reactant exhibited nonlinear change as the concentrations of Fe^{2+} or H_2O_2 increased. This could be attributed to the interactions between Fe^{2+} and H_2O_2 , where an excess of either Fe^{2+} or H_2O_2 could result in the inefficient consumption of each other. Moreover, the interaction between Fe^{2+} and H_2O_2 was also influenced by the concentration of organic reactant. Specifically, the optimized concentration ratio (i.e., the ratio at which the remaining pollutant concentration was lowest among all tested conditions) of Fe^{2+} to

H_2O_2 varied with the changes of pollutant concentrations, namely 1:2, 1:4, and 1:7 for 10, 50, and 100 mg L⁻¹, respectively.

S1.2 Impact of organic reactant type on reaction

The influence of the type of organic reactant was also analyzed. To highlight the influence of the type of organic reactant, the remaining concentration of the pollutants at the first sampling time (i.e., 2 min) was chosen as the performance metric, as this stage ensured sufficient Fe^{2+} and H_2O_2 . Moreover, an approximate estimation of the independent influence of the organic reactant type was obtained by normalizing the influence of reactant concentrations using the following equation:

$$I(\text{ORT}) = \frac{1}{m} \sum_{j=1}^m C(rc_j, \text{ORT}) \quad (2)$$

where I denotes the influence of reactant concentrations or organic reactant types. rc and ORT are a specific reactant concentration group and a variable representing the type of organic reactant, respectively.

As depicted in Figure S3a, in general, the phenolic pollutants with electron-withdrawing groups exhibited higher reaction rate compared to those with electron-donating groups. However, quantifying this relationship proved challenging and was subject to variations in reactant concentrations. For instance, alterations in the concentration parameters led to changes in the reaction rate order among different organic compounds (Figure S3b).

S2. Process of Fenton reactions

The Fenton experiments were conducted in a 25-mL reactor containing 20 mL of phenolic compound solution at specified concentrations. The temperature of solution was maintained at 20 °C using a cycle water cooler. The solution pH values were measured and adjusted to 3.0 ± 0.2 using 0.1 M H₂SO₄ at the beginning of reactions. The reaction was initiated by sequentially adding H₂O₂ and FeSO₄ solution with specified concentrations under vigorous stirring. At predefined time intervals (2, 5, 9, 15, 22, and 30 min), half a milliliter of the reaction solution was withdrawn and immediately quenched with half a milliliter of ascorbic acid solution (5 g L⁻¹). The concentrations of phenolic compounds were determined using an ultrahigh-performance liquid chromatograph (UPLC, 1290 Infinity II, Agilent Co., USA) equipped with a C18 column. The mobile phase was a mixture of acetonitrile and water containing 1‰ formic acid (5:95 for quinol and p-acetamidophenol, 10:90 for p-hydroxybenzyl alcohol, 20:80 for p-hydroxybenzoic acid, p-hydroxybenzaldehyde, p-hydroxyacetophenone and p-hydroxyanisole, 30: 70 for phenol, p-nitrophenol, methyl p-hydroxybenzoate and p-methylphenol, and 40:60 for p-chlorophenol v/v). The flow rate was 0.4 mL min⁻¹ and the detection wavelength was 273 nm for p-hydroxybenzyl alcohol, quinol and p-acetamidophenol, 280 nm for p-hydroxybenzoic acid, p-hydroxybenzaldehyde, p-hydroxyacetophenone, p-hydroxyanisole, phenol, methyl p-hydroxybenzoate, p-methylphenol and p-chlorophenol, and 320 nm for p-nitrophenol.

S3. Dimensionality reduction visualization and correlation analysis of kinetic profiles

S3.1 Dimensionality reduction visualization

S3.1.1 Methods of Dimensionality reduction visualization

To visually illustrate the differences in kinetic patterns within the dataset, we applied Principal Component Analysis (PCA) to project all kinetic curves onto a two-dimensional space. Specifically, each kinetic curve was represented as a vector ($\mathbb{R}^{1 \times 6}$), recording the reactant concentration at the initial time point and each sampling point (sampling scheme: 2, 5, 9, 15, 22, 30 min). To more accurately describe the shape of the kinetic curves, we computed their differential curves (i.e., the rate of concentration changes between consecutive time points), resulting in another vector ($\mathbb{R}^{1 \times 6}$). Each element of this vector represents the average reaction rate between two adjacent sampling points. These curves of all kinetic data collectively formed a matrix ($\mathbb{R}^{300 \times 6}$, where 300 corresponds to the number of samples). PCA was then applied to reduce the dimensionality of this matrix, yielding a two-dimensional matrix ($\mathbb{R}^{300 \times 2}$) representation for visualization in a two-dimensional space.

Furthermore, we applied the same projection method to kinetic curves following classical kinetic equations, including zero-order, first-order, second-order, and third-order kinetics. Specifically, we systematically varied the rate constant in the classical kinetic equations to generate a series of kinetic curves. When the rate constant is sufficiently large, the reactant concentration at the first sampling point (2 min) approaches zero. Increasing the rate constant beyond this point does not significantly alter the kinetic curve. Conversely, when the rate constant is very small, the reactant concentration at the final sampling point (30 min) remains close to the initial concentration. Further decreasing the rate constant will not affect the observed kinetic curve within the given sampling scheme. Thus, we defined the range of the rate constant as (0, k), where k is the critical value at which the reactant concentration at the first sampling point approaches zero. For instance, when the reactant concentration reaches $1/10^5$ of its initial value, it can be reasonably approximated as fully reacted, and increasing the rate constant further does not substantially alter the kinetic curve. Within this range, we generated a series of rate constants using an arithmetic sequence (e.g., step = 0.001) and computed the corresponding kinetic curves. These curves were then

subjected to PCA-based dimensionality reduction and visualized in the two-dimensional space, forming an approximate dashed trajectory. The points along this trajectory represent all kinetic curves that conform to the given kinetic equation, providing an intuitive classification standard for different reaction types.

S3.1.2 PCA dimensionality reduction

Given a matrix $X \in \mathbb{R}^{m \times n}$, where m is the number of samples (rows) and n is the number of features (columns). To remove mean bias from each feature, we subtract the mean of each column from the corresponding values to mean-centered data matrix \tilde{X} :

$$\tilde{x}_i = x_i - \frac{1}{m} \sum_{i=1}^m x_i \quad (3)$$

The covariance matrix $C \in \mathbb{R}^{n \times n}$ is computed as:

$$C = \tilde{X}^T \tilde{X} \quad (4)$$

Next, we perform eigen decomposition on the covariance matrix C , arrange the eigenvectors in descending order according to their eigenvalues, and select the top k eigenvectors to form the transformation matrix $P \in \mathbb{R}^{n \times k}$. Then, project the original data onto P to obtain the lower-dimensional representation $X' \in \mathbb{R}^{m \times k}$:

$$X' = \tilde{X}P \quad (5)$$

S3.1.3 Visualization analysis of the kinetic profiles

For the visualization, concentration-time profiles in the simulated dataset were projected onto a two-dimensional plane using principal component analysis,¹ where each point represents an individual profile. As illustrated in Figure S9a, the points were randomly scattered across the plane, reflecting the diverse kinetic patterns of different reactions. More importantly, most points deviated from the dotted lines that corresponded to the zero-, first-, second-, and third-order kinetic equations. This suggests that these traditional kinetic models were not sufficiently accurate to describe the complex kinetic patterns of the majority of the Fenton reactions.

S3.2 Correlation analysis

S3.2.1 Methods of Correlation Analysis

The pairwise Pearson correlation analysis was conducted between the pollutant concentrations from all reactions at each pair of sampling time points.

S3.2.2 Correlation analysis of the kinetic profiles

The correlation analysis (Figure S9b) revealed that there existed strong positive linear correlations ($r \geq 0.94$) between the concentrations of the reactant at adjacent sampling times. This is because the pollutants are degraded over time, meaning a higher remaining concentration at a certain time point tended to cause a higher concentration at later points. Furthermore, the pollutant concentrations were also strongly correlated with those at multiple earlier time points, indicating a persistent correlation over a wide time range. Based on these correlations, we proposed to use recursive relation to describe the pollutant concentrations over time, instead of traditional concentration-time equation. Given the inherent adaptability of recursive algorithms,^{2, 3} the as-constructed model was expected to perform well in capturing various kinetic patterns.

S4. Baseline models

S4.1 Macro-kinetic model (MA)

The commonly used macro-kinetic models were constructed based on zeroth-order (equation 6), first-order (equation 7), second-order (equation 8) and third-order (equation 9) kinetic equations.

$$\frac{C_t}{C_0} = kt \quad (6)$$

$$\ln\left(\frac{C_0}{C_t}\right) = kt \quad (7)$$

$$\left(\frac{1}{C_t} - \frac{1}{C_0}\right) = kt \quad (8)$$

$$\left(\frac{1}{2C_t^2} - \frac{1}{C_0^2}\right) = kt \quad (9)$$

where t represents the reaction time, k is the rate constant, C_0 is the initial concentration of the reactant, and C_t is the reactant concentration at time t .

The kinetic profiles can be fitted based on these equations using `scipy.optimize.curve_fit` (Figure S10).

For these macro-kinetic models, we evaluated their performance based on 5-fold cross-validation within the training set. It should be noted that they were explicit concentration–time equations, and thus only its fitting accuracy was assessed.

S4.2 Micro-kinetic model (MI)

For these micro-kinetic models, we evaluated their performance based on 5-fold cross-validation within the training set and predictive accuracy on the test set. It should be noted that MI₁ is an explicit concentration–time equation, and thus only its fitting accuracy was assessed (Figure S11). For MI₂, MI₃, and MI₄, we evaluated their fitting performance by individually fitting each kinetic curve in the training set (Figure S12). To assess their predictive performance, we fitted all training curves for each pollutant simultaneously using the corresponding equations to obtain a set of rate constants, which were then used to predict the degradation profiles in the test set (Figure S13).

S4.2.1 Construction of MI₁

The MI₁ was constructed referring to the procedures outlined by Wu et al.⁴ The

concentration-time equation of the reactant is expressed as follows:

$$bln\frac{[A]_0}{[A]_t} + a([A]_0 - [A]_t) = \frac{1}{c}(1 - e^{-ct}) \quad (10)$$

where a , b , c are the kinetic parameters. $[A]_t$ and $[A]_0$ denote the concentration of the reactant at t min and 0 min. t represents the reaction time.

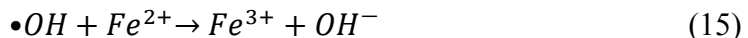
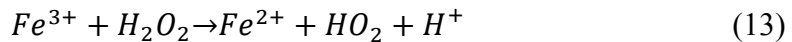
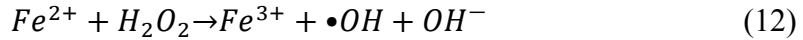
We further simplified the above expression using the ‘solve’ function in the Python package ‘sympy’ to the following form:

$$[A]_t = \frac{b}{a} LambertW\left(\frac{a}{b}e^{\frac{a-1}{bc} + \frac{1}{bc}e^{-ct}}\right) \quad (11)$$

The kinetic profiles can be fitted based on differential equation 11 using *scipy.optimize.curve_fit*.

S4.2.2 Construction of MI2

The MI₂ was constructed referring to the procedures outlined by Sun et al.⁵ The mechanism of Fenton is expressed as follows:



where P and P' denote the phenolic pollutant and reaction intermediates.

The kinetic behavior of the above reaction mechanism can be described by the following set of differential equations:

$$\frac{d[P]}{dt} = -k_5[P][\bullet OH] \quad (19)$$

$$\frac{d[Fe^{2+}]}{dt} = -k_1[Fe^{2+}][H_2O_2] + k_2[Fe^{3+}][H_2O_2] - k_4[Fe^{2+}][\bullet OH] + k_6[P'][Fe^{3+}] \quad (20)$$

$$\frac{d[H_2O_2]}{dt} = -k_1[Fe^{2+}][H_2O_2] - k_2[Fe^{3+}][H_2O_2] - k_3[\bullet OH][H_2O_2] - k_7[P'][H_2O_2] \quad (21)$$

$$\frac{d[\bullet OH]}{dt} = k_1[Fe^{2+}][H_2O_2] - k_3[\bullet OH][H_2O_2] - k_4[Fe^{2+}][\bullet OH] - k_5[\bullet OH][P] + k_7[P'][H_2O_2] \quad (22)$$

$$\frac{d[Fe^{3+}]}{dt} = k_1[Fe^{2+}][H_2O_2] - k_2[Fe^{3+}][H_2O_2] + k_4[Fe^{2+}][\bullet OH] - k_6[P'][Fe^{3+}]$$

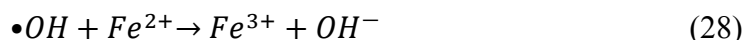
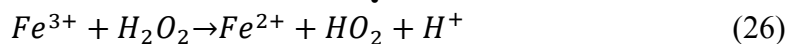
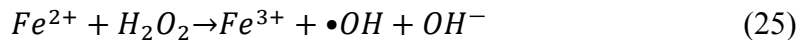
(23)

$$\frac{d[P']}{dt} = k_5[\bullet OH][P] - k_6[P'][Fe^{3+}] - k_7[P'][H_2O_2] \quad (24)$$

where $k_1, k_2, k_3, k_4, k_5, k_6$, and k_7 are rate constants of equation 12-18. The values of k_1, k_2, k_3 , and k_4 are 76, 3.16, 2.8×10^7 , and 4.3×10^8 M⁻¹ S⁻¹.⁵ Based on the pseudo steady state assumption, the concentration of reactive •OH radical will not vary with reaction time and its change rate was normally considered to approach zero ($\frac{d[\bullet OH]}{dt} = 0$).⁵ The values of k_5, k_6 , and k_7 were obtained by fitting experimental kinetic profiles, using python function *scipy.optimize.least_squares*.

S4.2.3 Construction of MI3

The MI₃ was constructed referring to the procedures outlined by De Heredia et al.⁶ The mechanism of Fenton is expressed as follows:



where P and P' denote the phenolic pollutant and reaction intermediates.

The kinetic behavior of the above reaction mechanism can be described by the following set of differential equations:

$$\frac{d[P]}{dt} = -k_6[P][\bullet OH] \quad (31)$$

$$\frac{d[Fe^{2+}]}{dt} = -k_1[Fe^{2+}][H_2O_2] + k_2[Fe^{3+}][H_2O_2] - k_4[Fe^{2+}][\bullet OH] \quad (32)$$

$$\frac{d[H_2O_2]}{dt} = -k_1[Fe^{2+}][H_2O_2] - k_2[Fe^{3+}][H_2O_2] - k_3[\bullet OH][H_2O_2] \quad (33)$$

$$\begin{aligned} \frac{d[\bullet OH]}{dt} &= k_1[Fe^{2+}][H_2O_2] - k_3[\bullet OH][H_2O_2] - k_4[Fe^{2+}][\bullet OH] - k_6[\bullet OH][P] \\ &\quad (34) \end{aligned}$$

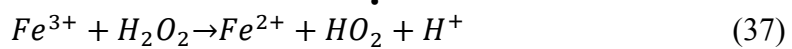
$$\frac{d[Fe^{3+}]}{dt} = k_1[Fe^{2+}][H_2O_2] - k_2[Fe^{3+}][H_2O_2] + k_4[Fe^{2+}][\bullet OH] \quad (35)$$

where k_1, k_2, k_3, k_4, k_5 , and k_6 are rate constants of equation 25-30. The values of k_1, k_2, k_3, k_4 , and k_5 are 76, 3.16, 2.8×10^7 , 4.3×10^8 and 1.3×10^6 M⁻¹ S⁻¹.⁵ Since k_5 is about two order smaller than k_4 , according to the literature,⁵ reactions (29) can be made unimportant. Based on the pseudo steady state assumption, the

concentration of reactive $\bullet\text{OH}$ radical will not vary with reaction time and its change rate was normally considered to approach zero ($\frac{d[\bullet\text{OH}]}{dt} = 0$).⁵ The values of k_6 was obtained by fitting experimental kinetic profiles, using python function *scipy.optimize.least_squares*.

S4.2.4 Construction of MI4

The MI₄ was constructed referring to the procedures outlined by Giménez et al.⁷ The mechanism of Fenton is expressed as follows:



where P denotes the phenolic pollutant and P' , P'' , and P''' denote reaction intermediates.

The kinetic behavior of the above reaction mechanism can be described by the following set of differential equations:

$$\frac{d[P]}{dt} = -k_4[P][\bullet\text{OH}] \quad (42)$$

$$\frac{d[\text{Fe}^{2+}]}{dt} = -k_1[\text{Fe}^{2+}][\text{H}_2\text{O}_2] + k_2[\text{Fe}^{3+}][\text{H}_2\text{O}_2] \quad (43)$$

$$\frac{d[\text{H}_2\text{O}_2]}{dt} = -k_1[\text{Fe}^{2+}][\text{H}_2\text{O}_2] - k_2[\text{Fe}^{3+}][\text{H}_2\text{O}_2] - k_3[\bullet\text{OH}][\text{H}_2\text{O}_2] \quad (44)$$

$$\begin{aligned} \frac{d[\bullet\text{OH}]}{dt} &= k_1[\text{Fe}^{2+}][\text{H}_2\text{O}_2] - k_3[\bullet\text{OH}][\text{H}_2\text{O}_2] - k_4[\bullet\text{OH}][P] - k_5[\bullet\text{OH}][P'] - k_6 \\ &[\bullet\text{OH}][P''] \end{aligned} \quad (45)$$

$$\frac{d[\text{Fe}^{3+}]}{dt} = k_1[\text{Fe}^{2+}][\text{H}_2\text{O}_2] - k_2[\text{Fe}^{3+}][\text{H}_2\text{O}_2] \quad (46)$$

$$\frac{d[P']}{dt} = k_4[\bullet\text{OH}][P] - k_5[P'][\bullet\text{OH}] \quad (47)$$

$$\frac{d[P'']}{dt} = k_5[P'][\bullet\text{OH}] - k_6[P''][\bullet\text{OH}] \quad (48)$$

where k_1 , k_2 , k_3 , k_4 , k_5 , and k_6 are rate constants of equation 36-41. The values of k_1 , k_2 , and k_3 are 76, 3.16, and $2.8 \times 10^7 \text{ M}^{-1} \text{ S}^{-1}$.⁵ Based on the pseudo steady state assumption, the concentration of reactive $\bullet\text{OH}$ radical will not vary with reaction time

and its change rate was normally considered to approach zero ($\frac{d[\bullet OH]}{dt} = 0$).⁵ The values of k_4 , k_5 , and k_6 were obtained by fitting experimental kinetic profiles, using python function `scipy.optimize.least_squares`.

S4.3 Machine learning macro-kinetic kinetic model (MLMA)

As shown in Figure 2b, the fitting error of the second-order kinetic equation was lower than those of the other three equations, as a result of which we selected it to construct the MAML₂ model.

A new machine learning model to predict the rate constants using the reaction conditions as inputs was trained, with its configurations detailed in Table S4. Using this model, the rate constant for the reactions under unknown conditions (i.e., the rate constants under these scenarios are not experimentally measured) can be predicted. Then, the kinetic profiles can be obtained by substituting the rate constants into the corresponding kinetic equations.

The evaluation results (Figure S14a and S14b) indicated that the model successfully predicted the rate constants for most reactions, except for a few individual cases. As for the prediction of kinetic profiles (Figure S14c), the mean absolute error (MAE) was 7.93%. The low accuracy of the MAML₂ model indicates its inability to address the complex kinetic patterns, demonstrating the ineffectiveness of the kinetic models directly adopting simple kinetic equations.

S4.4 Ablation baseline models

The RML model was derived from the MERML by removing the multiple estimation strategy. Its construction and evaluation followed the same methodology as the MERML, with the configurations summarized in Table S5.

The ML model (Figure S15) was derived from the MERML but not using the multiple estimation strategy and recursive algorithm. Its construction and evaluation also followed the same methodology as the MERML, with the configurations summarized in Table S6.

The MERLR was constructed by replacing the machine learning algorithm of the MERML with a linear regression algorithm, with the configurations summarized in Table S7.

S5. Evaluation of the application domain of the MERML for Fenton reaction

We demonstrated its potential for extension to the reactions under unknown reaction conditions, i.e., organic reactants not present in the training set and reactant concentrations outside the boundary values.

S5.1 Performance of model on Fenton reactions with unknown reactant concentrations

The potential application of the MERML to Fenton reactions under unknown reaction conditions, including unknown reactant concentrations and types of organic reactant, was assessed. Firstly, the model's applicability to unknown reactant concentrations was evaluated. The evaluation was conducted by using a leave-one-out experiment. Specifically, we iteratively selected one out of the 24 concentration conditions, treating the corresponding reaction data as the test set and the other data as the training set. The MERML, trained on the remaining reaction data, was then used to predict the performance of the reactions in the test set, and the prediction error was calculated. As shown in Table S9, the MERML demonstrated high accuracy ($R^2 > 0.80$) on most of the test sets, indicating its potential for application to reactions with unknown reactant concentrations. However, the model exhibited relatively lower accuracy ($R^2 \leq 0.80$) on a few test sets. This discrepancy may not be attributed to deficiencies in the MERML itself, but to the differences between the training and test sets. Specifically, the concentrations of Fe^{2+} or H_2O_2 in the test sets might be higher or lower than those in the corresponding training sets, which led to the tree model extrapolation failure. Therefore, the accuracy of the MERML on these test sets can be improved by reducing the gaps in reactant concentrations and expanding the amount of data in the training set.

S5.2 Performance of model on Fenton reactions of phenolic pollutants not present in training set

Moreover, the applicability of the MERML for phenolic pollutants not present in training set was also evaluated using a similar approach. We iteratively selected one out of the 12 types of reactants, using the reaction data of it as the test set and the other data as the training set. As shown in Table S10, the MERML demonstrated good accuracy ($R^2 > 0.80$) on five test sets, namely phenol, p-nitrophenol, p-hydroxybenzoic

acid, and p-hydroxyacetophenone. This indicated that the model had the potential to be applied to reactions involving unknown organic reactants. However, on the remaining seven test sets, the model exhibited poor accuracy, which could be attributed to the molecular descriptors employed during the data preprocessing. For instance, when reactions associated with p-chlorophenol were selected as the test set, the chlorine (Cl) atom, which has a significant impact on the properties of p-chlorophenol, was absent in the compounds present in the training set. Consequently, the model was impossible to recognize the influence of the Cl atom on the reaction based on the training data, resulting in inaccurate predictions for reactions involving p-chlorophenol. This issue can be greatly alleviated by employing more appropriate molecular descriptors and including a wider range of molecules in the training set.

S5.3 Performance of the MERML on Fenton reactions of other-type pollutants

Furthermore, we assessed the applicability of the MERML to non-phenolic pollutants. Kinetic data for the Fenton degradation of Drimaren Orange HF 2GL (DOHF, a reactive azo dye) and methyl parathion (MP, an organophosphorus pesticide) were extracted from the literature.^{8, 9} These data include initial reaction conditions—specifically temperature, pH, pollutant concentration, Fe²⁺ concentration, and H₂O₂ concentration—as well as the corresponding degradation kinetics (Table S11 and Figure S18). Although the original concentration–time profiles were not available, they were reconstructed using the Behnajady–Modirshahla–Ghanbery (BMG) model (Equation 49), which was reported to provide good fits to the experimental data.

$$\frac{t}{1 - \frac{C_t}{C_0}} = m + bt \quad (49)$$

where m and b are parameters to be fitted, t is the reaction time, and C_0 and C_t denote the pollutant concentration at the beginning of reaction and time t , respectively. The reconstructed dataset was used to retrain and evaluate the MERML, with detailed configurations provided in Table S12. The results (Figure S19) show that the model maintained high predictive accuracy, demonstrating its potential to generalize beyond phenolic compounds.

For future studies, expanding the dataset will further enhance the performance and generality of the model. Specific suggestions include: (i) incorporating a broader spectrum of contaminants beyond phenolic compounds, such as non-aromatic organics, halogenated aliphatics, multi-functional pesticides, pharmaceuticals, dyes, and

industrial chemicals; (ii) enriching the dataset with a wider range of pollutant concentrations and Fenton reagent dosages; and (iii) including experiments conducted under more complex reaction conditions, such as varied pH, temperature, and ionic strength. Such efforts will enable subsequent models to learn from more diverse scenarios and better predict the behavior of structurally diverse pollutants.

S6. Photocatalytic oxidation of bisphenol A (BPA)

S6.1 Dataset construction

This reaction was reported to follow the pseudo second-order kinetics (equation 8). Based on the equation and the rate constants (Table S13) obtained from the literature,¹⁰ we generated a series of kinetic profiles (with the sampling time as 10, 30, 60, 100, 150, and 210 min) through setting different initial concentrations of BPA (i.e., 1, 5, 10, 15, 20, 25, 30, 35, 40, 45, and 50 mg L⁻¹).

S6.2 Data preprocessing

For the other unspecified reaction parameters (i.e., conditions except for the concentration of BPA), we directly converted them into a one-hot vector. This vector was concatenated with the initial concentration of BPA to represent all the reaction parameters, which were then used as the inputs of the MERML.

S6.3 Model training and evaluation

The model was constructed and evaluated following the same procedures as in the *Model construction* section in the main text, with the configurations summarized in Table S14. As illustrated in Figure S20, the MERML exhibited precise prediction of the kinetic profiles of BPA in this reaction.

Supplementary Figures

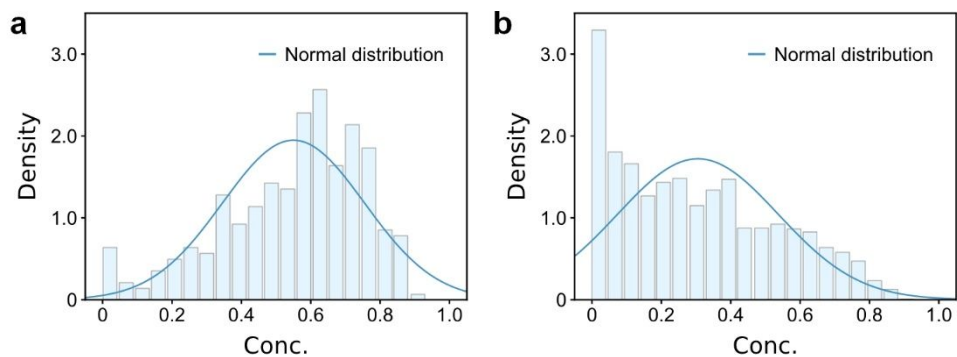


Figure S1. Data distribution of remaining concentrations of organic reactant at the first (a) and all (b) sampling points.

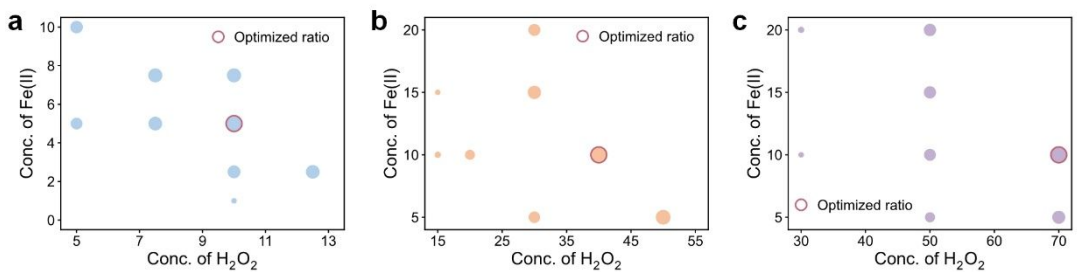


Figure S2. Impact of reactant concentrations on reaction performance. The initial organic reactant concentrations were 10 (a), 50 (b), and 100 (c) mg L^{-1} .

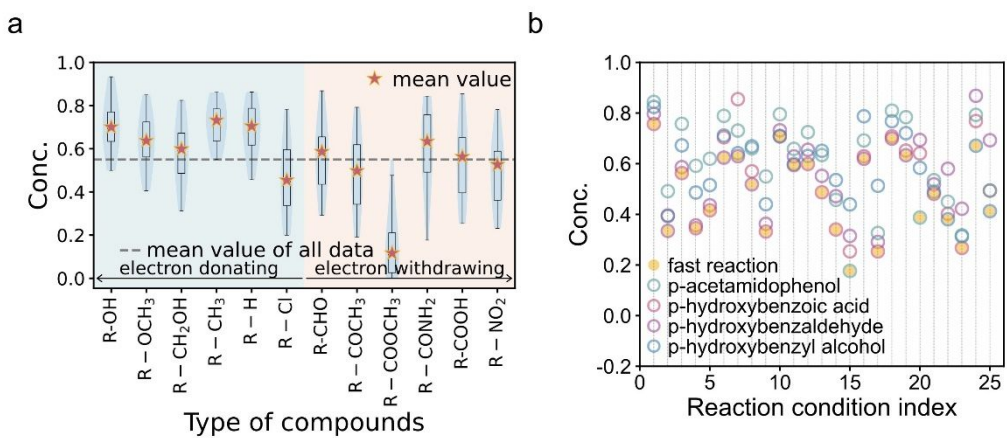


Figure S3. Impact of organic reactant type on reaction performance. (a) Distribution of remaining concentrations at 2 min for different organic reactants. R- represents the 4-OH-C₆H₄- group. (b) Remaining concentrations in different reactant concentration groups for four specific organic reactants.

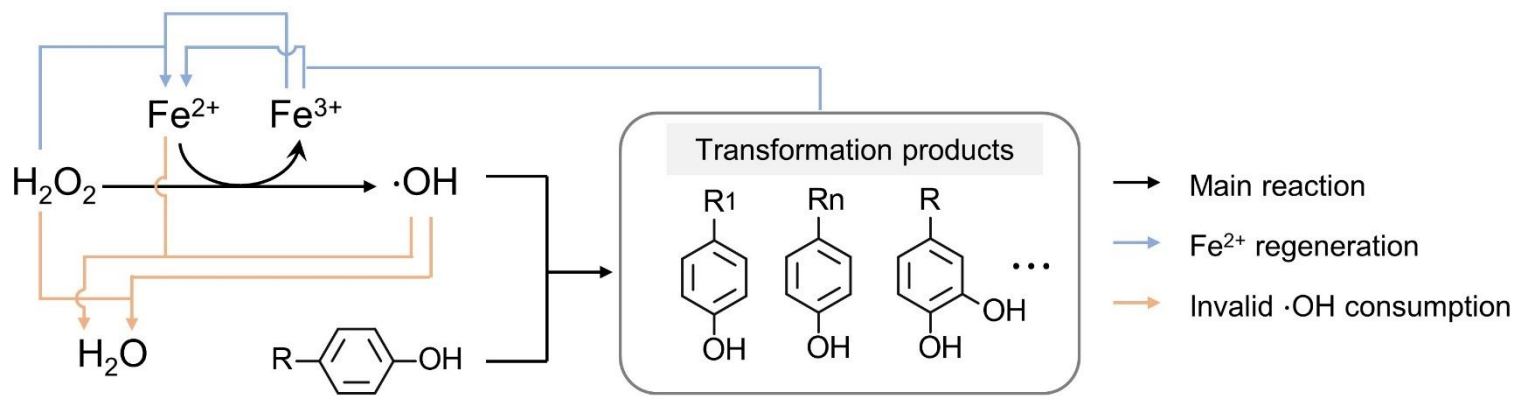


Figure S4. Main reaction mechanism of the Fenton reaction of phenolic compounds.

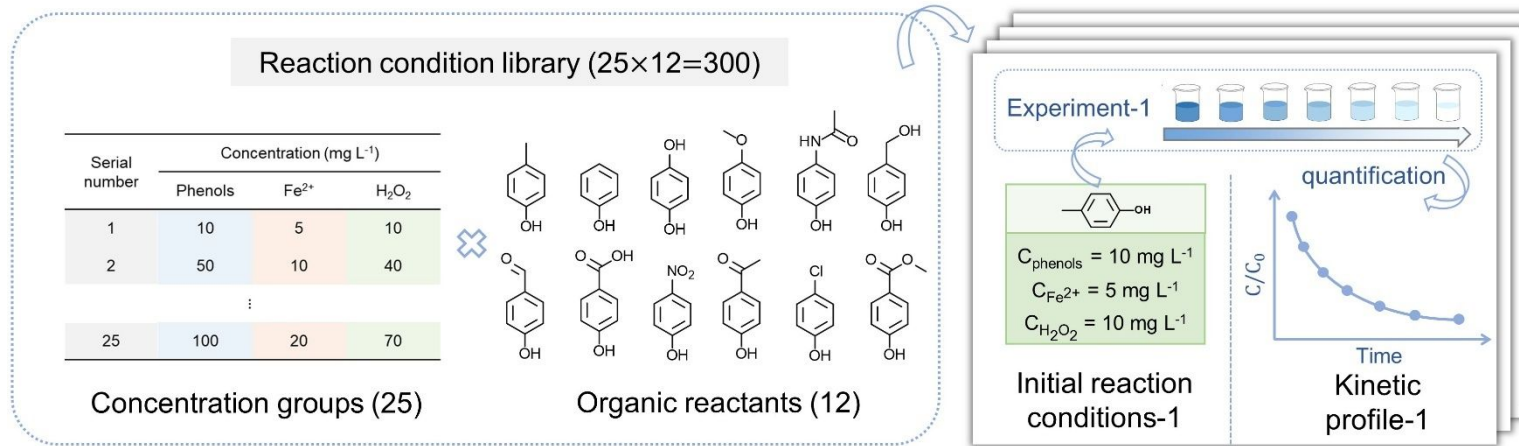


Figure S5. Workflow of the dataset construction.

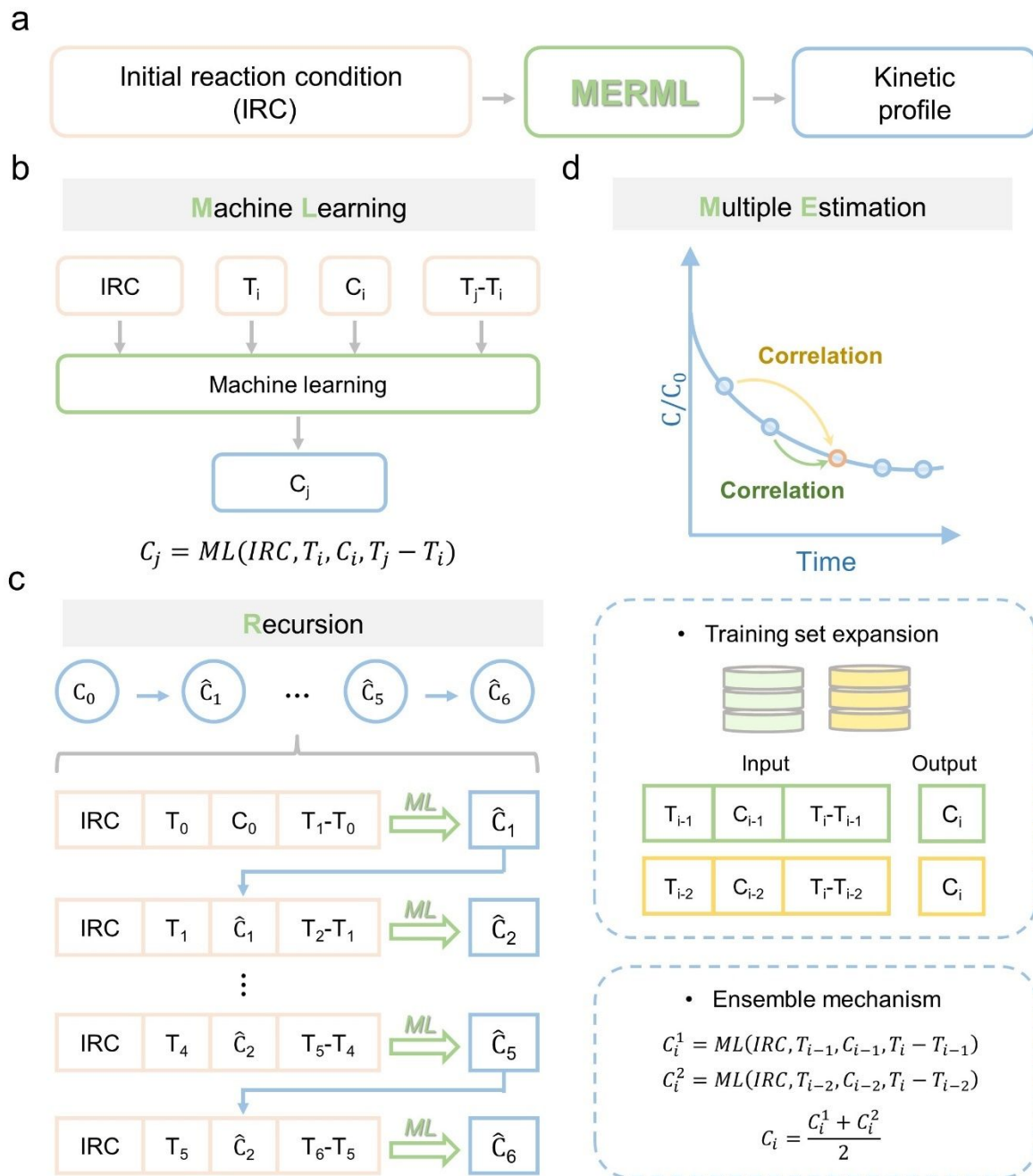


Figure S6. Model architecture and the construction workflow of the MERML framework. (a) Inputs and outputs of the MERML framework. (b) Machine learning model for predicting single-timepoint concentration in the MERML framework. (c) Recursive process of predicting the entire kinetic profile. (d) Illustration of the multiple estimation strategy (taking $k = 2$ as an example).

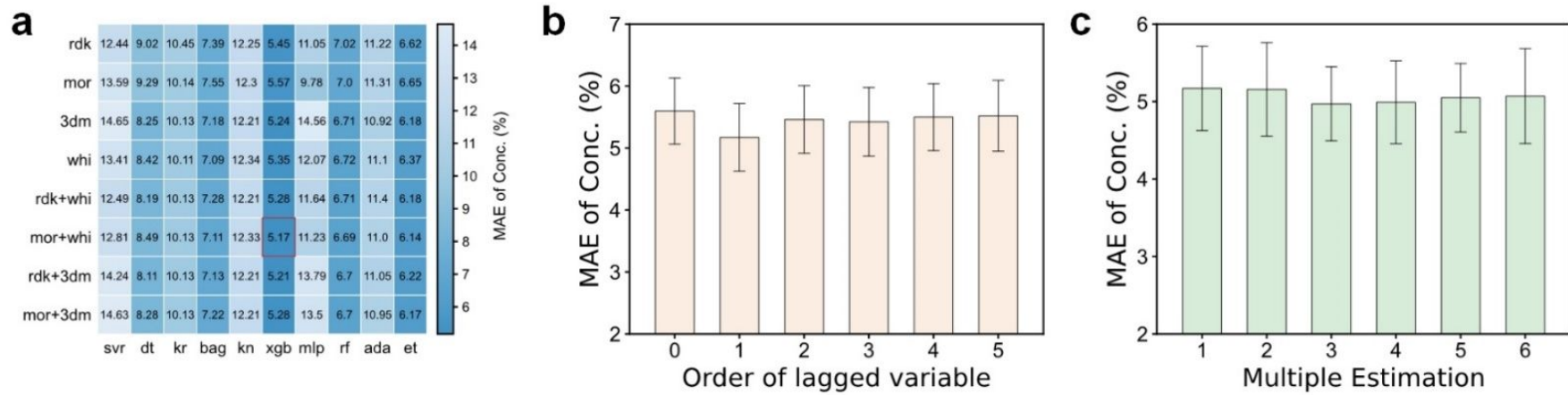


Figure S7. Determination of basic components of the ERML model. (a) Accuracy of the ERML model using different combinations of molecular descriptors and machine learning algorithms with 1-order lagged variable and once estimation. rdk: RDKit fingerprints; mor: Morgan fingerprints; 3dm: 3D-Morse molecular descriptors; whi: WHIM molecular descriptors. svr: supporting vector machine; dt: decision tree; kr: kernel ridge; bag: bagging; kn: k-nearest neighbors; xgb: XGBoost; mlp: multi-layer perceptron; rf: random forest; ada: adaboost; et: extreme tree. (b) Accuracy of the ERML model using different orders of the lagged variable (the number of previous reaction states used), with the number of estimations as 1. (c) Accuracy of the ERML model using different numbers of estimation, with the optimal number of estimations as 3.

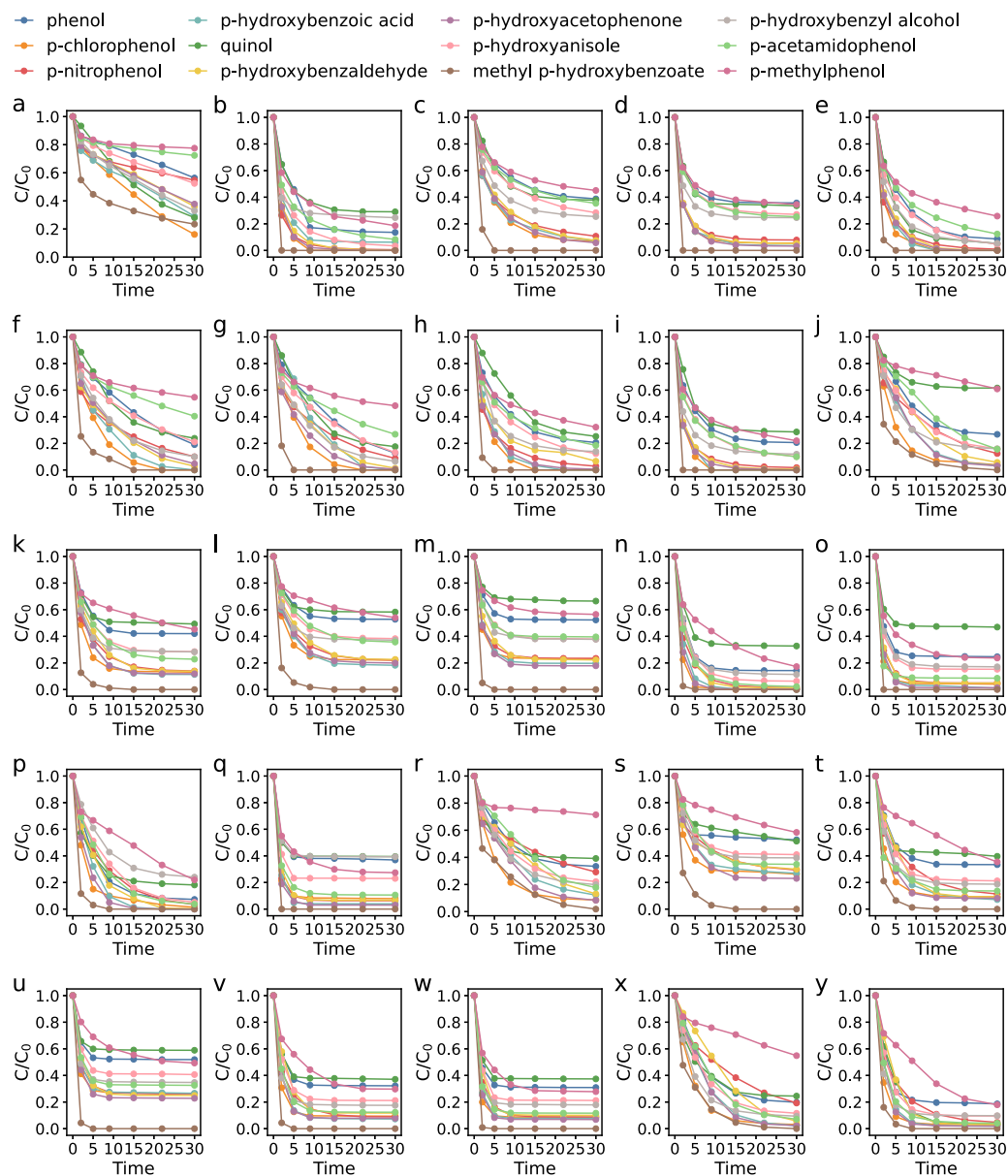


Figure S8. Raw kinetic profiles of the Fenton reactions. The reagent concentration combinations of the panels are displayed in Table S3.

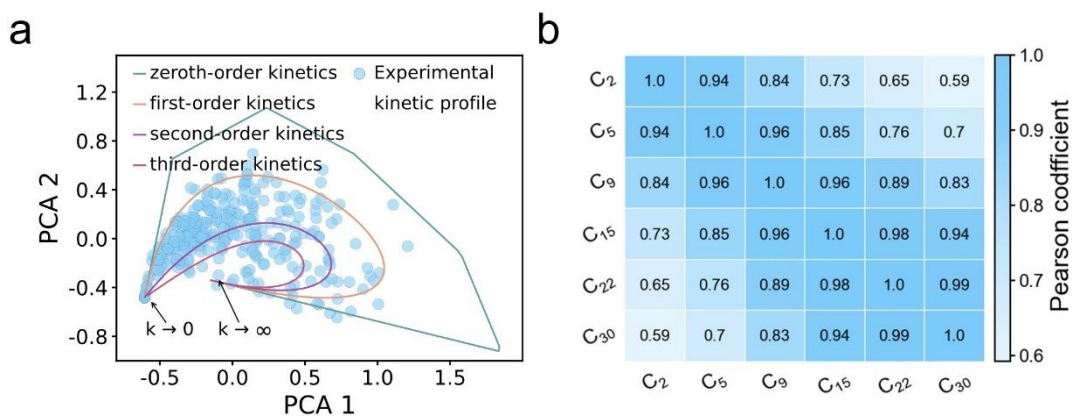


Figure S9. Visualization and correlation analysis of the kinetic data and modeling inspiration obtained from it. (a) Dimension reduction visualization of the kinetic profiles via principal component analysis (PCA). Details of this figure were described in Text S3. (b) Correlations among the reactant concentrations at different reaction time points. C_i: the relative concentration of phenolic pollutants at Ti (Ti = 2, 5, 9, 15, 22, 30 min).

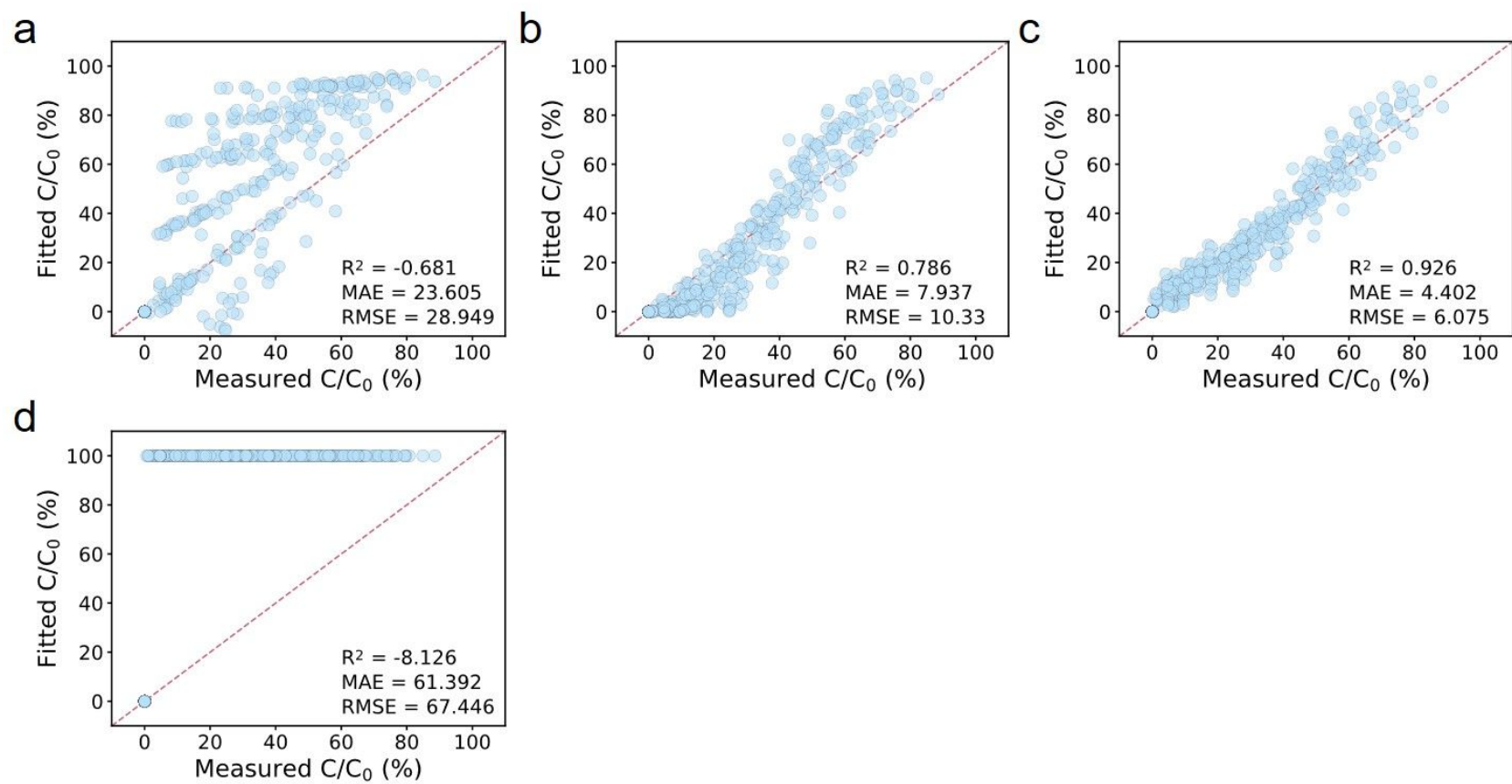


Figure S10. Fitting performances of MA₀ (a), MA₁ (b), MA₂ (c), and MA₃ (d) on the test set.

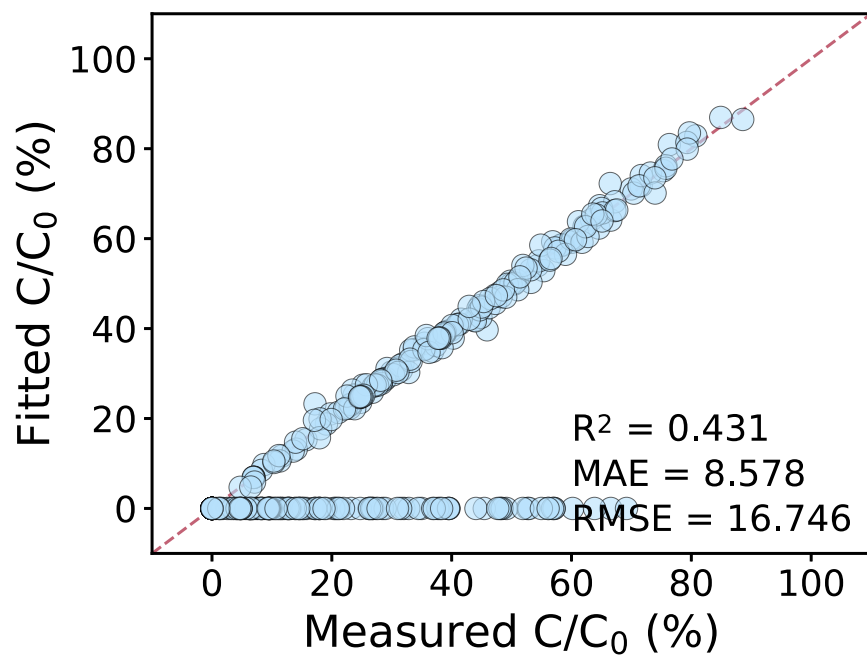


Figure S11. Fitting performances of MI₁ on the test set.

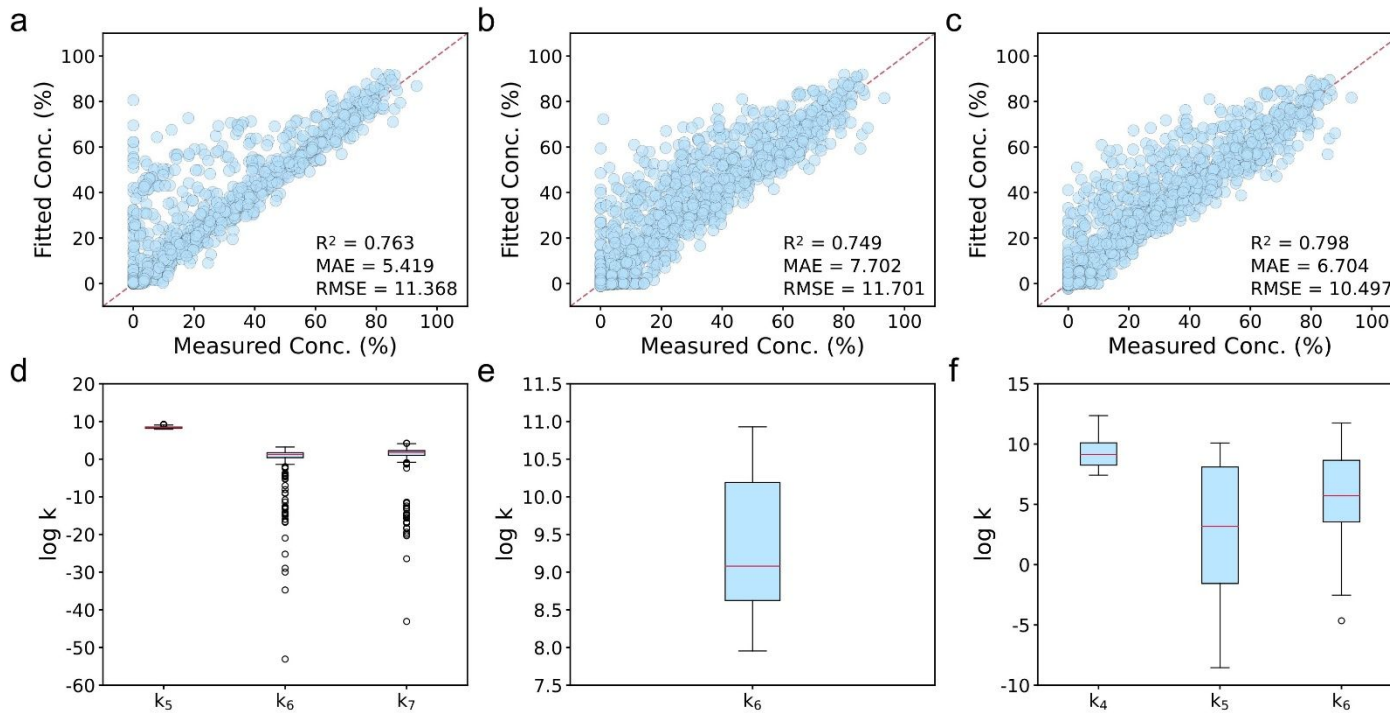


Figure S12. (a–c) Fitting performance of the micro-kinetic models MI₂ (a), MI₃ (b), and MI₄ (c), where the unknown rate constants were obtained by fitting the kinetic profiles for each experimental condition separately. (d–f) Distribution of the fitted rate constants obtained from the models MI₂ (d), MI₃ (e), and MI₄ (f).

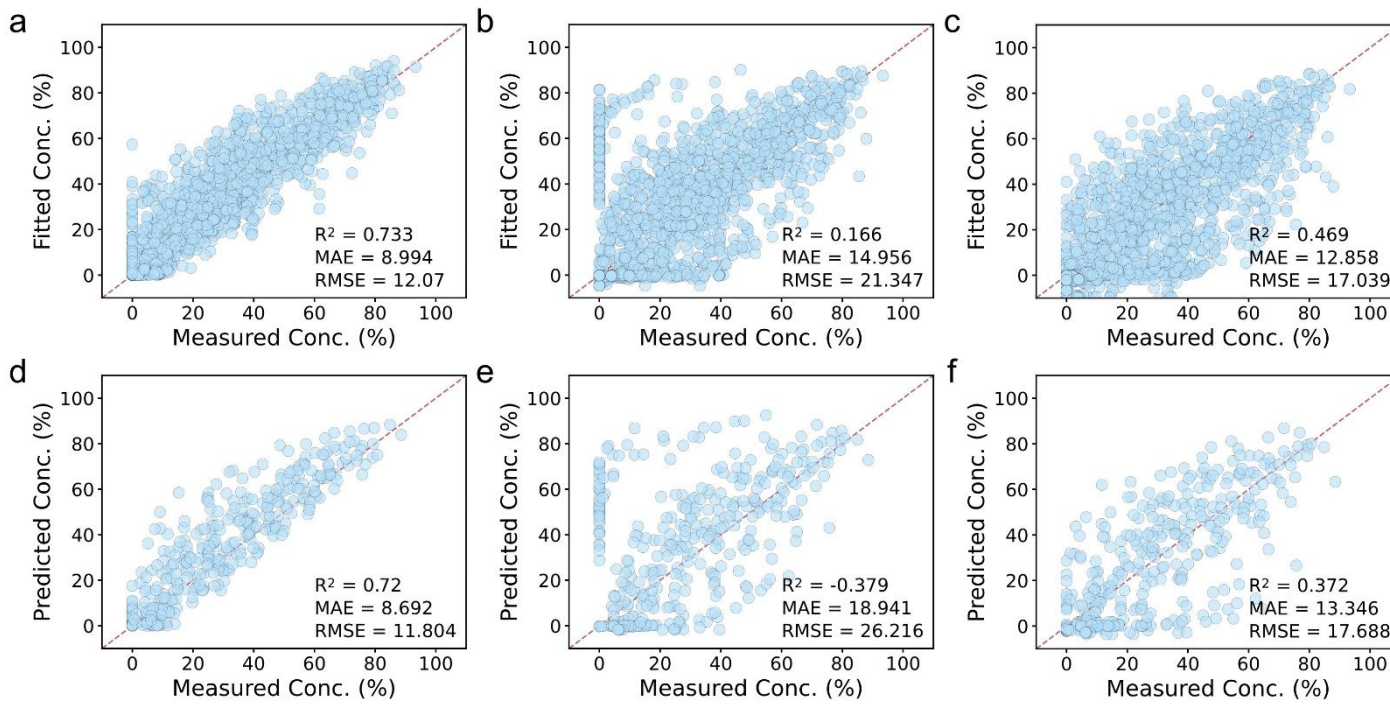


Figure S13. (a–c) Fitting performance of the micro-kinetic models MI₂ (a), MI₃ (b), and MI₄ (c) using a global fitting approach, in which all experimental conditions were fitted simultaneously to obtain a single set of rate constants. (d–f) Predictive performance of MI₂ (d), MI₃ (e), and MI₄ (f) on the test sets based on the globally fitted parameters.

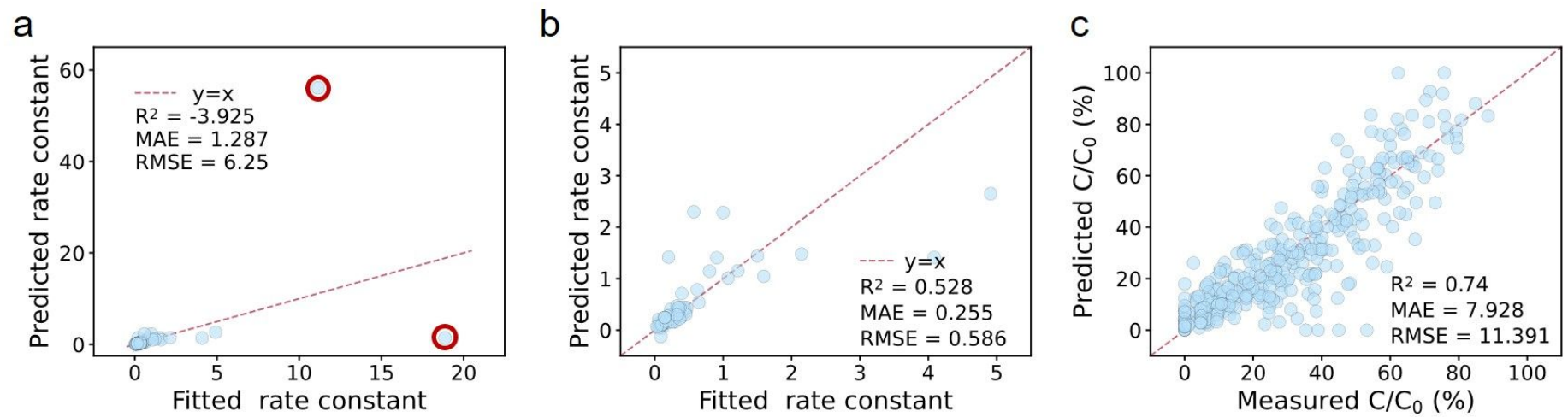


Figure S14. The rate constant prediction result of MB model. (a) Rate constant prediction results of all the reactions in the test set. The red circle marked the two points with the top 2 largest prediction error. (b) Rate constant prediction results of the reactions in the test set after removing reactions with the top 2 largest prediction error. (c) Predicting performance of the MLMA₂ model on the test set.

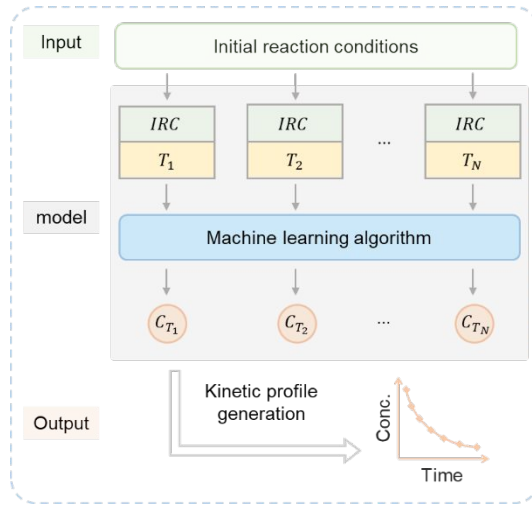


Figure S15. Architecture of the ML model. *IRC*: initial reaction conditions. T_i : time of the i -th sampling point ($i = 1, 2, \dots, N$). C_{T_i} : relative concentration of the organic reactant at T_i .

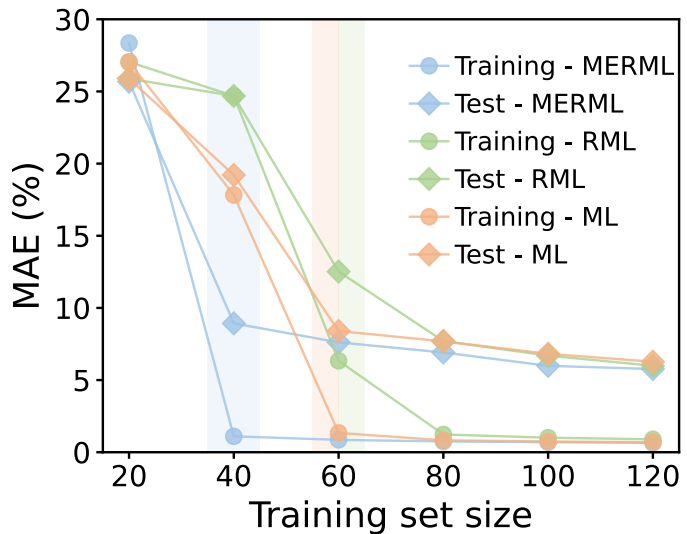


Figure S16. Performance of the MERML, RML, and ML model on the training and test set, when trained with dataset of different sizes.

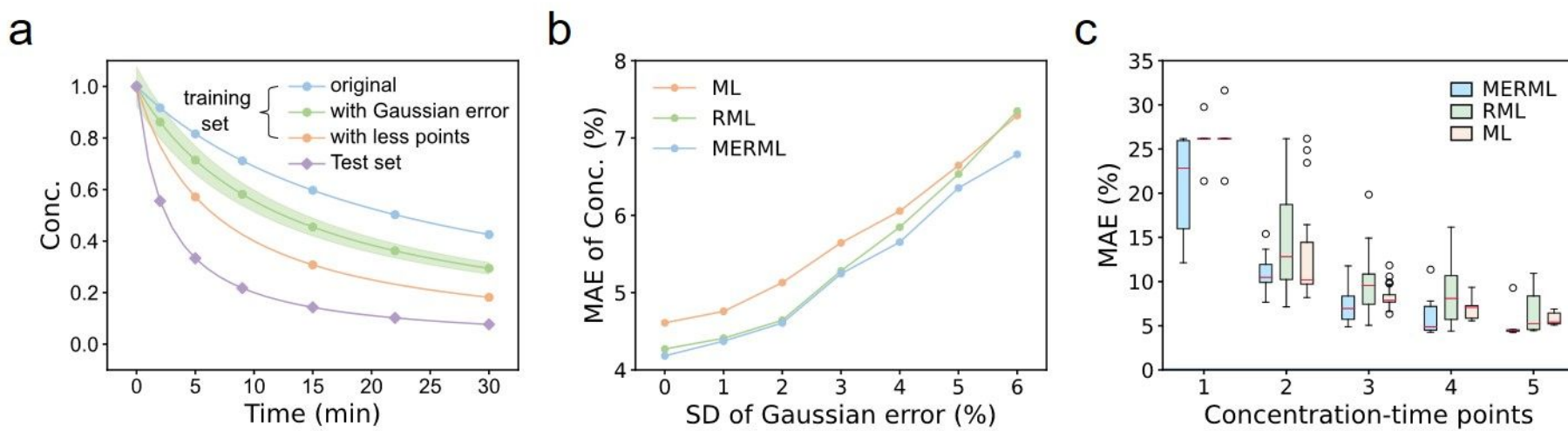


Figure S17. Evaluation method and result of the robustness of the MERML. (a) Training sets used for robustness evaluation. For the scenario involving experimental noise, the MERML was trained on a modified dataset in which Gaussian noise was manually introduced into the kinetic profiles. For the scenario with missing concentration–time points, the MERML was trained on datasets where 1 to 5 points were randomly removed from the original 6-point kinetic profiles. (b) Performance of the MERML on the test set when involving experimental noise. (c) Performance of the MERML on the test set when missing concentration–time points.

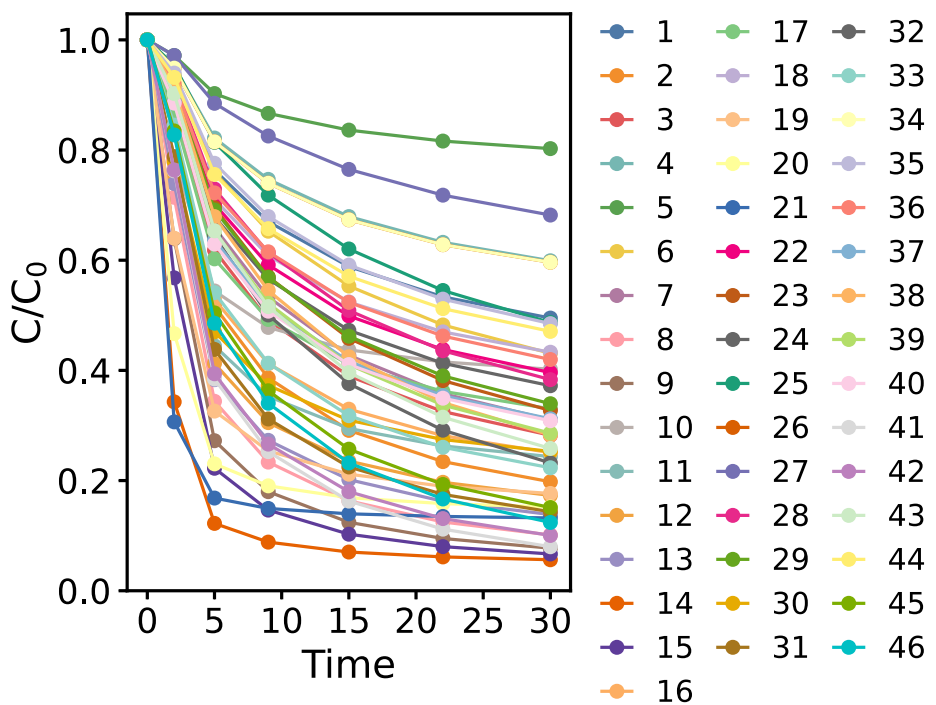


Figure S18. Kinetic profiles in the supplementary dataset described in Text S5.3. The legend corresponds to the index in Table S11.

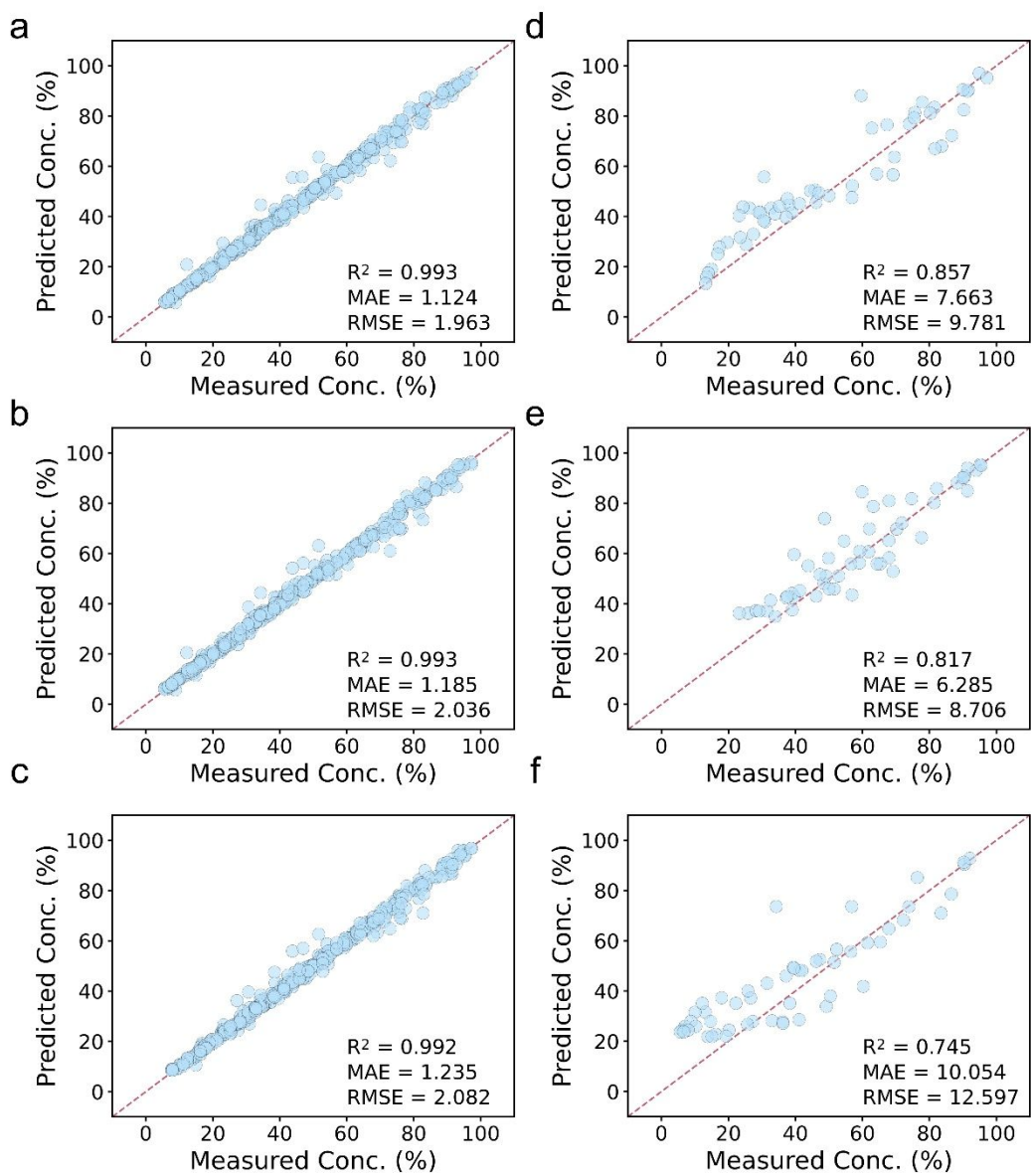


Figure S19. Prediction performance of MERML on Fenton reactions of DOHF and MP. Panels a/d, b/e, and c/f correspond to the results obtained from different random splits of the training and test sets.

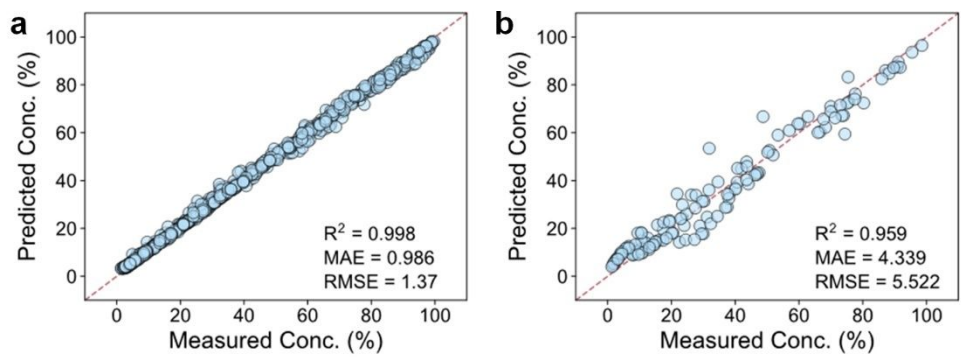


Figure S20. Regression performance of the MERML for the photocatalytic degradation of bisphenol A. a) Training set. b) Test set.

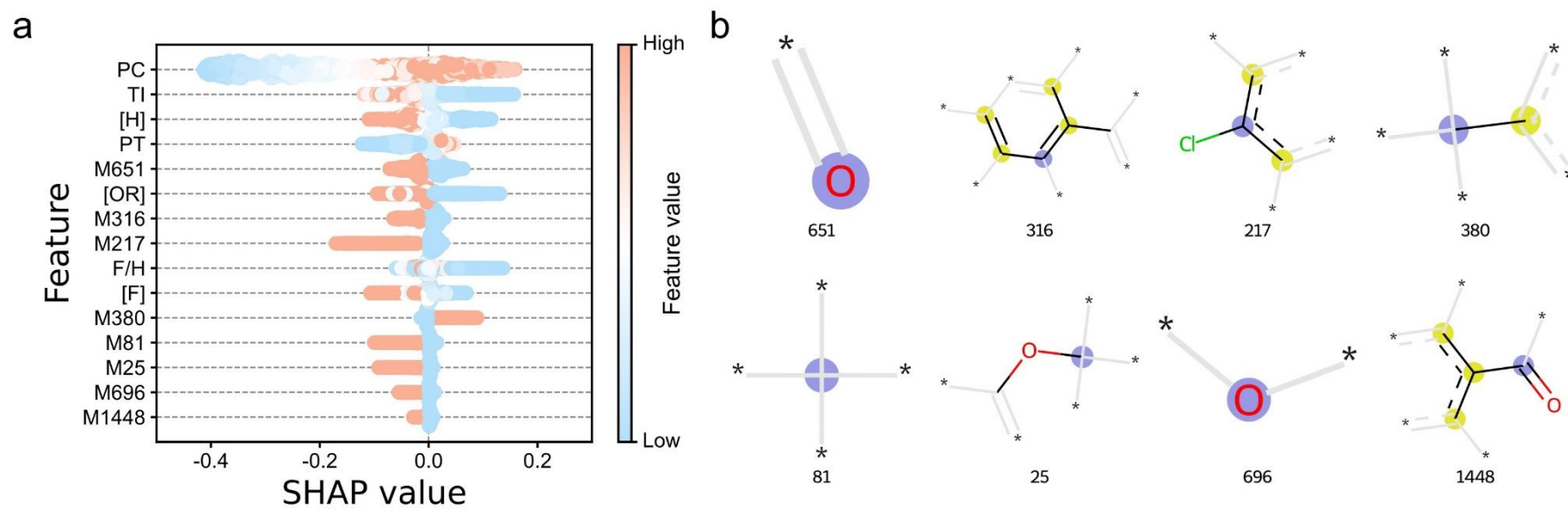


Figure S21. Mechanistic explanation in terms of chemical structure. (a) Contributions of top 15 important features on all samples, ranking from top to down according to the importance. PC: previous organic reactant concentration; [H]: initial concentration of H_2O_2 ; TI: time interval; [OR]: initial concentration of organic reactant; PT: previous reaction time; F/H: the ratio of initial concentration of Fe^{2+} to that of H_2O_2 ; [F]: initial Fe^{2+} concentration; M-num: the num-th bit in Morgan fingerprints. (b) Specific structures of the Morgan molecular descriptors in the top 15 important features. The background colors purple and yellow indicate the central atom in the environment and aromatic atoms, respectively. The symbol '*' indicates arbitrary atom.

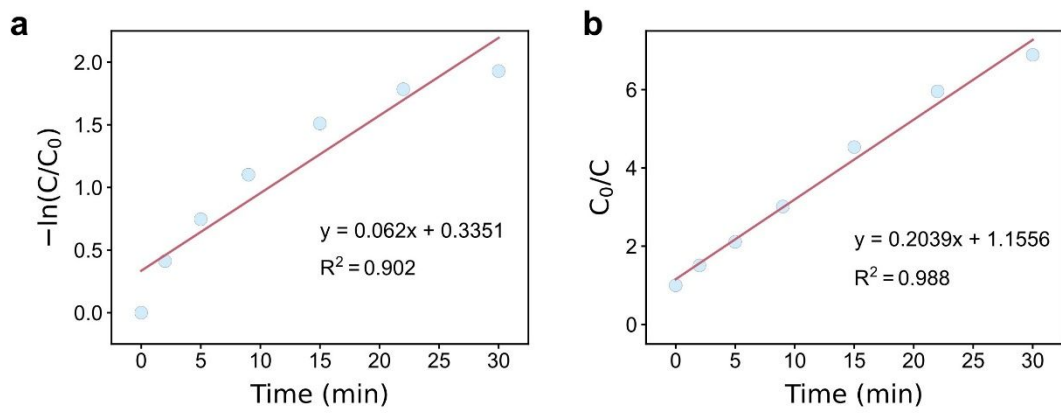


Figure S22. First-order a) and second-order b) kinetics fitting of the kinetic profile in orange in Figure 5f.

Supplementary Tables

Table S1. Specific inputs of the MERML for the Fenton reaction.

Weighted holistic invariant molecular descriptors ¹¹						The i-th bit in Morgan fingerprint descriptors				Reaction parameters
L1u	E2m	G3e	G1i	Te	Du	25	562	1091	1657	[OR]
L2u	E3m	E1e	G2i	Tp	Dm	81	651	1108	1684	[F]
L3u	L1v	E2e	G3i	Ti	Dv	92	673	1149	1716	[H]
P1u	L2v	E3e	E1i	Ts	De	100	695	1153	1739	F/H
P2u	L3v	L1p	E2i	Au	Dp	127	696	1179	1755	PT
G1u	P1v	L2p	E3i	Am	Di	146	707	1181	1758	TI
G2u	P2v	L3p	L1s	Av	Ds	185	716	1196	1769	PC
G3u	G1v	P1p	L2s	Ae	Vu	188	754	1217	1810	
E1u	G2v	P2p	L3s	Ap	Vm	192	777	1270	1821	
E2u	G3v	G1p	P1s	Ai	Vv	208	839	1275	1824	
E3u	E1v	G2p	P2s	As	Ve	217	849	1283	1849	
L1m	E2v	G3p	G1s	Gu	Vp	246	876	1335	1850	
L2m	E3v	E1p	G2s	Gm	Vi	286	890	1355	1918	
L3m	L1e	E2p	G3s	Ku	Vs	316	919	1386	1933	
P1m	L2e	E3p	E1s	Km		323	932	1448	1937	
P2m	L3e	L1i	E2s	Kv		380	936	1479	1964	
G1m	P1e	L2i	E3s	Ke		408	1005	1537	2034	
G2m	P2e	L3i	Tu	Kp		457	1036	1576		
G3m	G1e	P1i	Tm	Ki		516	1058	1593		
E1m	G2e	P2i	Tv	Ks		540	1088	1622		

† [OR], [F] and [H] are the initial concentrations of organic reactants, Fe^{2+} and H_2O_2 , respectively. F/H is the ratio between the initial concentrations of Fe^{2+} and H_2O_2 . PT and PC are the reaction time and the conversion at previous sampling point. TI is the time interval between previous and current sampling points.

Table S2. Configurations of the MERML for the Fenton reaction.

Inputs	Multiple estimation strategy	Algorithm	Hyper-parameters			
			eta	round	max depth	min child weight
Concentrations of organic compound, Fe^{2+} and H_2O_2						
Ratio of the concentrations between Fe^{2+} and H_2O_2						
Vector for organic compound type encoded using Morgan ¹² fingerprint and WHIM ¹¹ descriptors	3-time estimation	XGBoost	0.1	600	8	18
Previous reaction state (i.e., previous reactant concentrations and reaction time)						
Time intervals						

† The hyper-parameters were obtained by grid search.

Table S3. Reagent concentration combinations of the Fenton reactions of phenolic compounds.

Index	Pollutant	Fe ²⁺ concentration	H ₂ O ₂ concentration
	concentration (mg/L)	(mg/L)	(mg/L)
1	10	1	10
2	10	7.5	10
3	10	5	5
4	10	10	5
5	10	5	10
6	10	2.5	10
7	10	2.5	12.5
8	10	5	7.5
9	10	10	5
10	50	5	30
11	50	10	20
12	50	10	15
13	50	15	15
14	50	10	40
15	50	15	30
16	50	5	50
17	50	20	30
18	100	5	50
19	100	10	30
20	100	10	50
21	100	20	30
22	100	15	50
23	100	20	50
24	100	5	70
25	10	10	70

† Index 1-25 are corresponding to the panel a-y in Figure S5.

Table S4. Configurations of the rate constant prediction model in MLMA₂.

	Reactant concentrations	[OR], [F], [H], and F/H
Inputs	Molecular descriptors	combination RDKit fingerprint and 3D-Morse
Algorithm	XGBoost	
Hyper-parameters	default value in python package (xgboost=1.5.1)	

†[OR], [F] and [H] were the initial concentrations of organic reactant, Fe²⁺ and H₂O₂; F/H: the ratio of the concentrations between Fe²⁺ and H₂O₂, respectively. 3D-Morse: 3D molecular representations of structure based on electron diffraction descriptors.

Table S5. Configurations of the RML model.

Inputs	Algorithm	Hyper-parameters			
		eta	round	max depth	min child weight
Concentrations of organic compound, Fe^{2+} and H_2O_2					
Ratio of the concentrations between Fe^{2+} and H_2O_2	XGBoost	0.1	900	5	4
Reaction types encoded into one-hot vector					
Previous reaction state (i.e., previous reactant concentrations and reaction time)					
Time intervals					

† The hyper-parameters were obtained by grid search.

Table S6. Configurations of the ML model.

Inputs	Algorithm	Hyper-parameters			
		eta	round	max depth	min child weight
Concentrations of organic compound, Fe^{2+} and H_2O_2					
Ratio of the concentrations between Fe^{2+} and H_2O_2	XGBoost	0.1	700	5	6
Reaction types encoded into one-hot vector					
Reaction time					

† The hyper-parameters were obtained by grid search.

Table S7. Configurations of the MERLR model.

Inputs	Algorithm	Multiple estimation strategy
Concentrations of organic compound, Fe^{2+} and H_2O_2		
Ratio of the concentrations between Fe^{2+} and H_2O_2	Linear regression	5-time estimation
Reaction types encoded into one-hot vector		
Previous reaction state (i.e., previous reactant concentrations and reaction time)		
Time intervals		

† The hyper-parameters were obtained by grid search.

Table S8. Application domain of the MERML for the Fenton reaction.

Variables	Range	Possible values in the dataset
Concentration of organic reactants	10-100 mg L ⁻¹	10, 50, 100 mg L ⁻¹
Concentration of Fe ²⁺	1-20 mg L ⁻¹	1, 2.5, 5, 7.5, 10 mg L ⁻¹ (for the organic reactants of 10 mg L ⁻¹) 5, 10, 15, 20 mg L ⁻¹ (for the organic reactants of 50 and 100 mg L ⁻¹) 5, 7.5, 10, 12.5 mg L ⁻¹ (for the organic reactants of 10 mg L ⁻¹)
Concentration of H ₂ O ₂	5-70 mg L ⁻¹	15, 20, 30, 40, 50 mg L ⁻¹ (for the organic reactants of 50 mg L ⁻¹) 30, 50, 70 mg L ⁻¹ (for the organic reactants of 100 mg L ⁻¹)
Type of organic reactants	-	p-hydroxyanisole, p-acetamidophenol, p-hydroxybenzyl alcohol, p-nitrophenol p-hydroxybenzaldehyde, p-chlorophenol, p-hydroxybenzoic acid, p-methylphenol, p-hydroxyacetophenone, quinol, methyl p-hydroxybenzoate, phenol

Table S9. Performance of the MERML for the Fenton reaction under unknown reactant concentrations.

OR	Initial concentrations in test sets			Metrics		
	F	H	R^2	MAE	RMSE	
10	1	10	-1.467	0.258	0.290	
10	2.5	10	0.650	0.128	0.148	
10	2.5	12.5	0.940	0.047	0.062	
10	5	5	0.808	0.082	0.097	
10	5	7.5	0.915	0.045	0.066	
10	5	10	0.642	0.090	0.116	
10	7.5	7.5	0.940	0.032	0.045	
10	7.5	10	0.822	0.049	0.073	
10	10	5	0.892	0.049	0.059	
50	5	30	0.933	0.044	0.058	
50	5	50	0.816	0.086	0.114	
50	10	15	0.775	0.076	0.092	
50	10	20	0.859	0.053	0.077	
50	10	40	0.056	0.162	0.200	
50	15	15	0.971	0.019	0.028	
50	15	30	0.902	0.043	0.055	
50	5	30	0.897	0.031	0.044	
100	5	50	0.266	0.177	0.224	
100	5	70	0.098	0.217	0.244	
100	10	30	0.946	0.034	0.047	
100	10	50	0.648	0.106	0.119	
100	10	70	0.599	0.085	0.112	
100	15	50	0.959	0.031	0.041	
100	20	30	0.887	0.041	0.054	

† OR: organic reactant; H: H_2O_2 ; F: Fe^{2+} ; the unit of the concentrations was mg L^{-1} .

Table S10. Performance of the MERML for the Fenton reaction of phenolic pollutants not present in training set.

Organic reactant type in test sets	R^2	MAE	RMSE
p-acetamidophenol	-0.829	0.263	0.302
methyl p-hydroxybenzoate	-7.935	0.294	0.331
p-chlorophenol	0.305	0.139	0.149
p-hydroxyacetophenone	0.899	0.046	0.062
p-nitrophenol	0.950	0.039	0.046
p-hydroxybenzaldehyde	0.772	0.092	0.104
p-hydroxybenzyl Alcohol	0.566	0.089	0.116
p-hydroxyanisole	0.553	0.113	0.131
p-hydroxybenzoic acid	0.865	0.065	0.078
p-methylphenol	0.044	0.134	0.178
phenol	0.854	0.060	0.074
quinol	0.577	0.100	0.123

Table S11. Reaction conditions in the supplementary dataset of the Fenton reaction of DOHF and MP.

Index	Pollutant	pH	Fe ²⁺ (mg/L)	H ₂ O ₂ (mg/L)	C ₀ (mg/L)	T (°C)	Ref.
1	DOHF	2	10.0	0.20	200	20	
2	DOHF	3	10.0	0.20	200	20	
3	DOHF	4	10.0	0.20	200	20	
4	DOHF	5	10.0	0.20	200	20	
5	DOHF	6	10.0	0.20	200	20	
6	DOHF	3	5.0	0.20	200	20	
7	DOHF	3	7.5	0.20	200	20	
8	DOHF	3	15.0	0.20	200	20	
9	DOHF	3	20.0	0.20	200	20	
10	DOHF	3	15.0	0.03	200	20	
11	DOHF	3	15.0	0.05	200	20	⁹
12	DOHF	3	15.0	0.08	200	20	
13	DOHF	3	15.0	0.10	200	20	
14	DOHF	3	15.0	0.10	50	20	
15	DOHF	3	15.0	0.10	100	20	
16	DOHF	3	15.0	0.10	300	20	
17	DOHF	3	15.0	0.10	400	20	
18	DOHF	3	15.0	0.10	300	10	
19	DOHF	3	15.0	0.10	300	30	
20	DOHF	3	15.0	0.10	300	40	
21	DOHF	3	15.0	0.10	300	50	
22	MP	2	40.0	2.22	30	25	
23	MP	3	40.0	2.22	30	25	⁸
24	MP	4	40.0	2.22	30	25	
25	MP	5	40.0	2.22	30	25	

26	MP	6	40.0	2.22	30	25
27	MP	7	40.0	2.22	30	25
28	MP	3	502.0	11.43	30	25
29	MP	3	502.0	13.88	30	25
30	MP	3	502.0	16.67	30	25
31	MP	3	502.0	19.42	30	25
32	MP	3	502.0	22.21	30	25
33	MP	3	502.0	24.97	30	25
34	MP	3	502.0	27.76	30	25
35	MP	3	201.0	22.21	30	25
36	MP	3	302.0	22.21	30	25
37	MP	3	402.0	22.21	30	25
38	MP	3	603.0	22.21	30	25
39	MP	3	704.0	22.21	30	25
40	MP	3	804.0	22.21	30	25
41	MP	3	502.0	22.21	10	25
42	MP	3	502.0	22.21	20	25
43	MP	3	502.0	22.21	40	25
44	MP	3	502.0	22.21	30	15
45	MP	3	502.0	22.21	30	35
46	MP	3	502.0	22.21	30	45

Table S12. Configurations of the MERML for the Fenton reactions of DOHF and MP.

Inputs	Algorithm	Hyper-parameters				
		eta	round	max depth	min child weight	
Concentrations of pollutant, Fe^{2+} and H_2O_2						
Ratios of the concentrations between pollutant and Fe^{2+} , pollutant and pollutant and Fe^{2+} , as well as Fe^{2+} and H_2O_2						
Temperature	XGBoost	0.1	100	5	5	
pH						
Reaction types encoded into one-hot vector						
Previous reaction state (i.e., previous reactant concentrations and reaction time)						
Time intervals						

† The hyper-parameters were obtained by grid search.

Table S13. Rate constants of the photocatalytic reaction extracted from the literature.¹⁰

Reaction	Rate constant ($\times 10^{-3}$ L mg ⁻¹ min ⁻¹)
R1	1.112
R2	1.274
R3	1.640
R4	2.337
R5	7.220
R6	0.399
R7	1.140
R8	3.577
R9	0.981
R10	4.748

Table S14. Configurations of the MERML for the photocatalytic reaction.

Inputs	Multiple estimation strategy	Algorithm	Hyper-parameters			
			eta	round	max depth	min child weight
Concentrations of reactant						
Reactant types encoded into one-hot vector						
Previous reaction state (i.e., previous reactant concentrations and reaction time)	2-time estimation	XGBoost	0.02	200	7	4
Time intervals						

† The hyper-parameters were obtained by grid search.

Table S15. Configurations of the MERML for analysis of the impact of Fenton reagent dosage ratios pollutant types (Figure 5c and 5d).

Inputs	Multiple estimation strategy	Algorithm	Hyper-parameters			
			eta	round	max depth	min child weight
Concentrations of organic compound, Fe ²⁺ and H ₂ O ₂						
Ratio of the concentrations between Fe ²⁺ and H ₂ O ₂						
Organic compound type encoded into one-hot vectors	3-time estimation	XGBoost	0.1	600	8	18
Previous reaction state (i.e., previous reactant concentrations and reaction time)						
Time intervals						

† The hyper-parameters were set according to the hyper-parameters in Table S2.

Table S16. Configurations of the MERML for analysis of the impact of chemical structures (Figure S21).

Inputs	Multiple estimation strategy	Algorithm	Hyper-parameters			
			eta	round	max depth	min child weight
Concentrations of organic compound, Fe ²⁺ and H ₂ O ₂						
Ratio of the concentrations between Fe ²⁺ and H ₂ O ₂						
Organic compound type encoded by Morgan fingerprints	3-time estimation	XGBoost	0.1	600	8	18
Previous reaction state (i.e., previous reactant concentrations and reaction time)						
Time intervals						

† The hyper-parameters were set according to the hyper-parameters in Table S2.

Table S17. Phenolic compounds contained the chemical structures in the top 15 important features in Figure S21a.

Compound	Chemical structure							
	M651	M316	M217	M380	M81	M25	M696	M1448
R-OH								
R-OCH ₃					✓		✓	
R-CH ₂ OH								
R-CH ₃				✓				
R-H								
R-Cl			✓					
R-CHO	✓							✓
R-COCH ₃	✓	✓				✓	✓	
R-COOR	✓	✓						
R-CONH ₂	✓							
R-COOH	✓	✓						
R-NO ₂	✓							✓

† R- represents the 4-OH-C₆H₄- group. ✓ indicates the chemical structure was contained in the compounds.

REFERENCES

- (1) Greenacre, M.; Groenen, P. J. F.; Hastie, T.; D'Enza, A. I.; Markos, A.; Tuzhilina, E., Principal component analysis. *Nat Rev Methods Primers* **2022**, *2* (1), 100.
- (2) Li, H.; Wu, Y.; Chen, M.; Lu, R., Adaptive multigradient recursive reinforcement learning event-triggered tracking control for multiagent systems. *IEEE Trans. Neural Networks Learn. Syst.* **2021**, *34* (1), 144-156.
- (3) Kavis, A.; Skoulakis, S.; Antonakopoulos, K.; Dadi, L. T.; Cevher, V., Adaptive stochastic variance reduction for non-convex finite-sum minimization. *Adv. Neural Inform. Process. Syst.* **2022**, *35*, 23524-23538.
- (4) Wu, Y.; Zhou, S.; Qin, F.; Zheng, K.; Ye, X., Modeling the oxidation kinetics of Fenton's process on the degradation of humic acid. *J. Hazard. Mater.* **2010**, *179* (1), 533-539.
- (5) Sun, J.-H.; Sun, S.-P.; Fan, M.-H.; Guo, H.-Q.; Qiao, L.-P.; Sun, R.-X., A kinetic study on the degradation of p-nitroaniline by Fenton oxidation process. *J. Hazard. Mater.* **2007**, *148* (1-2), 172-177.
- (6) De Heredia, J. B.; Torregrosa, J.; Dominguez, J. R.; Peres, J. A., Kinetic model for phenolic compound oxidation by Fenton's reagent. *Chemosphere* **2001**, *45* (1), 85-90.
- (7) Giménez, B. N.; Conte, L. O.; Audino, F.; Schenone, A. V.; Graells, M.; Alfano, O. M.; Pérez-Moya, M., Kinetic model of photo-Fenton degradation of paracetamol in an annular reactor: main reaction intermediates and cytotoxicity studies. *Catalysis Today* **2023**, *413-415*, 113958.
- (8) Saini, R.; Kumar Mondal, M.; Kumar, P., Fenton oxidation of pesticide methyl parathion in aqueous solution: kinetic study of the degradation. *Environmental Progress & Sustainable Energy* **2016**, *36* (2), 420-427.
- (9) Değermenci, N.; Değermenci, G. D.; Ulu, H. B., Decolorization of reactive azo dye from aqueous solutions with Fenton oxidation process: effect of system parameters and kinetic study. *Desalination Water Treat.* **2019**, *169*, 363-371.
- (10) Yang, C.; Wang, P.; Li, J.; Wang, Q.; Xu, P.; You, S.; Zheng, Q.; Zhang, G., Photocatalytic PVDF ultrafiltration membrane blended with visible-light responsive Fe(III)-TiO₂ catalyst: Degradation kinetics, catalytic performance and reusability. *Chem. Eng. J.* **2021**, *417*, 129340.
- (11) Todeschini, R.; Consonni, V., Descriptors from Molecular Geometry. In *Handbook of*
S-58

Chemoinformatics, 2003; pp 1004-1033.

- (12) Rogers, D.; Hahn, M., Extended-Connectivity Fingerprints. *J. Chem. Inf. Model.* **2010**, *50* (5), 742-754.